Journal of Power Sources 320 (2016) 153–167

Contents lists available at ScienceDirect

Journal of Power Sources

journal homepage: www.elsevier.com/locate/jpowsour

Microscale characterisation of stochastically reconstructed carbon fiber-based Gas Diffusion Layers; effects of anisotropy and resin content

Andreas G. Yiotis*, Michael E. Kainourgiakis, Georgia C. Charalambopoulou, Athanassios K. Stubos

Environmental Research Laboratory, NCSR 'Demokritos', 15310 Athens, Greece

HIGHLIGHTS

- We propose a novel algorithm for resin deposition in GDLs.
- We obtain microscale information using X-ray micro-CT measurements.
- We study the transport properties of realistic reconstructed GDLs.
- We focus primarily on the effects of resin content and medium anisotropy.
- Our numerical calculations compare very good with experimental data.

ARTICLE INFO

Article history:
Received 14 January 2016
Received in revised form
4 April 2016
Accepted 20 April 2016
Available online 28 April 2016

Keywords:
Gas Diffusion Layer
PEM fuel cell
Permeability
Diffusivity
Conductivity

ABSTRACT

A novel process-based methodology is proposed for the stochastic reconstruction and accurate characterisation of Carbon fiber-based matrices, which are commonly used as Gas Diffusion Layers in Proton Exchange Membrane Fuel Cells. The modeling approach is efficiently complementing standard methods used for the description of the anisotropic deposition of carbon fibers, with a rigorous model simulating the spatial distribution of the graphitized resin that is typically used to enhance the structural properties and thermal/electrical conductivities of the composite Gas Diffusion Layer materials. The model uses as input typical pore and continuum scale properties (average porosity, fiber diameter, resin content and anisotropy) of such composites, which are obtained from X-ray computed microtomography measurements on commercially available carbon papers. This information is then used for the digital reconstruction of realistic composite fibrous matrices. By solving the corresponding conservation equations at the microscale in the obtained digital domains, their effective transport properties, such as Darcy permeabilities, effective diffusivities, thermal/electrical conductivities and void tortuosity, are determined focusing primarily on the effects of medium anisotropy and resin content. The calculated properties are matching very well with those of Toray carbon papers for reasonable values of the model parameters that control the anisotropy of the fibrous skeleton and the materials resin content.

1. Introduction

Proton Exchange Membrane Fuel Cells Fuel Cells (PEMFCs) are compact electrochemical energy conversion devices consisting of stacks of several layers of materials that perform different highly specialized functions (Fig. 1). The reacting gases (typically H_2 and O_2) are introduced into the Membrane Electrode Assembly (MEA), the core of the system, through appropriately designed flow channels (bipolar plates) and diffuse towards the catalytic electrodes, where the electrochemical reactions take place to generate electricity [1]. The diffusion of the reactants from the flow channels to the catalyst layers is facilitated by a highly porous and tortuous, electrical conductive layer, namely the Gas Diffusion Layer (GDL), with a typical thickness of a few hundreds of microns [2]. GDLs are placed between the flow channels and the electrodes (anode and cathode) on both sides of the MEA and their properties related to

* Corresponding author.
E-mail address: yiotis@ipta.demokritos.gr (A.G. Yiotis).

http://dx.doi.org/10.1016/j.jpowsour.2016.04.096
0378-7753/

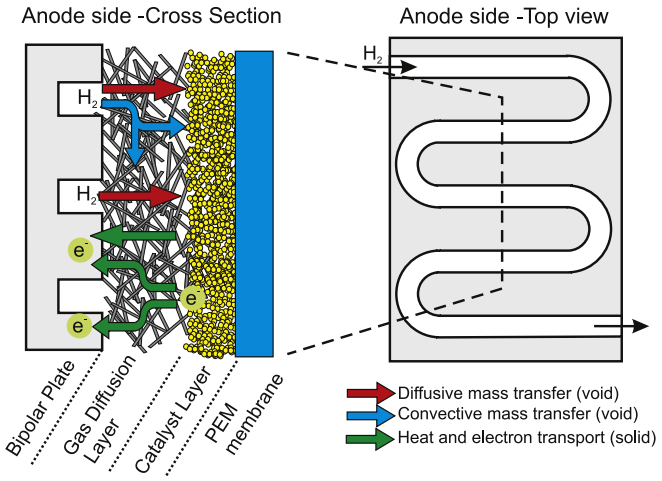

Fig. 1. Schematic of dominant transport mechanisms through the Gas Diffusion Layer at the cross-section of the anode side of a PEM fuel cell. H_2 flows through the channels of the bipolar plane and is transferred towards the catalytic surfaces by diffusion (primarily in the through-plane direction) and convection (primarily in the in-plane direction). The electrical current and heat flow in the opposite direction from the catalyst towards the ribs of the bipolar plate. Higher in-plane conductivities allow for the enhanced collection of electrons and heat from regions of the catalyst surface that are not directly below the ribs.

flow, mass transfer, thermal and electrical conductivity, constitute a crucial parameter for the efficient operation of PEMFC units.

GDLs combine particular transport and structural properties (such as high porosity and permeability to flow) that allow for the efficient flow and mass transport of the reacting species towards the electrodes, even below the ribs of the bipolar plates (that are not in direct contact with the flow channels (Fig. 1)), thus significantly extending their active electrocatalytic surface [2]. GDLs also exhibit excellent electrical and thermal conductivity for the efficient removal of the electrons and heat produced at the catalytic electrodes towards the ribs of the bipolar plates, as well as significant structural strength under compression, which is typically applied to ensure gas-tight conditions [3]. It is thus clear that GDL characteristics are quite essential for the optimization of the PEMFCs' design and the improvement of their performance.

The typical types of materials currently used as GDLs in PEMFCs, include carbon-based materials (such as woven carbon cloths, non-woven carbon papers, carbon foams) or metal-based materials (e.g. meshes, metal foams and other micromachined metal substrates) [4]. The vast majority, however, of GDLs in commercially-available PEMFCs are made of Carbon fiber-based (C-fiber) papers, primarily due to their relative easy and low-cost fabrication from conventional papermaking processes using polyacrilonitrile (PAN) filaments with a typical diameter of 12–14 μm [5]. After carbonizing the filaments at temperatures of 1200–1350 °C, the carbon fibers are chopped into smaller pieces (3–12 mm long) and dispersed into water with polyvinyl alcohol that serves as a binding agent. The film produced after drying is impregnated with a carbonizable, typically thermosetting, resin (e.g. phenolic) that allows for the formation of a fabric-type material at the desired thickness and density. The resin content of this intermediate material typically ranges between 50 and 70% w/w [2]. At the final stage of the production process, heating at temperatures well above 2000^{o}C is applied resulting in the graphitization of the C-fiber-resin composite and significantly enhancing the robustness, but also the transport properties of the finished product. During this step, the material loses approx. 40% of its initial weight, with a greater weight loss originating from the resin component, rather than the already carbonized C-fiber skeleton. While accurate measurements are still lacking in the literature, it may be expected that the resin content of the finished product lies between 10 and 30% w/w. The above production route is currently adopted by manufacturers such as Toray Industries Inc., while other methods are also available (including the use of PTFE powder to bind the material and increase the contact area between fibers, instead of resin impregnation and graphitization) [2].

The accurate determination of the transport properties of such C-fiber/ resin composites is a field of very active research in recent years. A series of studies, both experimental [6–11] and numerical [12,13], have been devoted to the investigation of several important continuum-scale (macroscopic) properties, including permeabilities, thermal and electrical conductivities, also addressing the variation of these features at the in-plane/through-plane directions due to the material's anisotropy. The numerical studies reported so far have focused on the microscale reconstruction of the fibrous matrix for the direct solution of transport equations at the pore scale and the calculation of spatial averages over larger material samples. In this context, different material reconstruction methods have been proposed including pore networks [14,15], Voronoi tesselations [16], but also process-based methods for the representation of the spatial distribution of the individual components of the composite (fibers and resin) [17–20]. The latter, process-based, concept has proven quite successful in reproducing structures that are at least qualitatively similar with the images of the actual material obtained from electron microscopy (e.g. SEM) and/or microtomographic imaging methods (e.g. X-ray μ-CT). The determination of the spatial distribution of the resin component, however, still remains an open challenge, since most of the proposed methods are based on a rather phenomenological approach of morphological opening, that relies on placing spheres of increasing radii in the fibrous skeleton to mimic the wetting behavior of the resin [21,22]. The precise determination of the resin's spatial distribution is in fact a crucial parameter for the accurate calculation of key transport properties of the material, and primarily those related to the through-plane cross-sectional area between fibrous layers, such as thermal and electrical conductivities. However the results of the numerical studies that have attempted so far to address this topic, are quite scattered, and often significantly diverging from experimental data. Those discrepancies have been attributed to the uncertainty related to the bulk phase properties of the two components (resin and fibers), rather than the domain reconstruction method itself [12,19–21].

In the present work we propose a novel process-based methodology for the realistic, stochastic reconstruction of composite carbon fiber/resin matrices, by combining standard algorithms for the anisotropic deposition of carbon fibers [23] with a rigorous resin model hat has significant advantages over conventional approaches, as it allows to obtain realistic, physically meaningful spatial distributions of the graphitized resin based only on very few adjustable parameters. The latter pursues the minimization of the interfacial energy of the system through a stochastic phase redistribution algorithm, which physically describes the wetting process taking place during the impregnation of the fibrous matrix with the resin. In order to be able to arrive to realistic digital domains with this methodology, we first performed X-ray computed microtomography (μ-CT) measurements on commercially available carbon papers to deduce their typical pore and continuum scale properties (average porosity, fiber diameter, resin content, anisotropy). This information is further used for the digital reconstruction of the carbon paper samples, where we solve the corresponding conservation equations at the microscale in order to determine their effective transport properties, such as Darcy permeabilities, effective diffusivities, thermal/electrical conductivities and void

tortuosity, focusing primarily on their variation as a result of the medium's anisotropy and resin content. We demonstrate that the proposed methodology describes quite satisfactorily, compared to literature experimental data, the entire range of transport properties, both in-plane and through-plane, for reasonable values of the key reconstruction parameters (material's porosity, fiber diameter, medium anisotropy, resin content).

2. 3D X-ray micro-CT imaging of a commercial C-fiber paper

A series of 3D X-ray μ-CT scans of material samples obtained from a single 10 x 10 cm^2 sheet of Toray TGP-H-090 carbon paper (without PTFE treatment) purchased from FuelCell Store were performed using a Bruker Skyscan 1272 system. The specimens had a typical size of ~2 $\times$ 1 mm^2 and the scanning resolution was 1 μm/pixel. The obtained images were post-processed using the open-source Fiji-ImageJ software in order to filter image noise and facilitate the reconstruction of the digitized 3D domains to be used for numerical modeling. The 3D stacks were subsequently cropped to remove image margins and binarized using the default ImageJ thresholds. The void volume fraction in all samples was found to be between 0.77 and 0.79, in agreement with the porosity of ~0.78 reported by the manufacturer [24].

Fig. 2 shows the top and cross-sectional view of a scanned sample. The average thickness of the specimen was measured to be 285 μm, also in agreement with the value of 280 μm provided by the manufacturer [24]. These images clearly reveal the structural characteristics of the medium, that consists of straight carbon fibers with a diameter in the range of 7–9 μm, glued together with a resin that appears to behave as a wetting phase, covering primarily the regions of fiber intersections and smaller pores. The fibers are mainly oriented in the xy-plane (in-plane) with a random, however, direction within this plane.

A rough estimate of the sample's anisotropy was obtained using

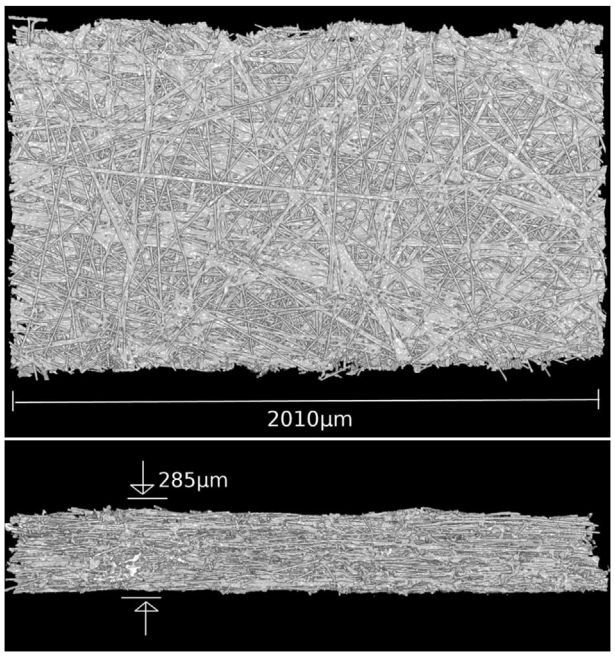

Fig. 2. Top and side view of a 3D reconstructed sample of Toray TGP-H-090 carbon paper (without PTFE treatment) obtained with μ-CT imaging at a 1 μm/pixel resolution. The paper consists of C-fibers with a diameter of 7–9 μm, glued together with a carbon-based resin covering primarily the regions of fiber intersections. The fibers are primarily oriented in the x-y plane (in-plane) with a random however direction within this plane.

the ImageJ Skeletonize plugin. The produced fiber skeleton was subsequently analyzed using the Analyze Skeleton plugin that identifies all skeleton branches (fiber segments between intersections) and reports the position vectors of their edges $\vec{r}_1 = (x_1, y_1, z_1)$ and $\vec{r}_2 = (x_2, y_2, z_2)$, and the total branch length L. The results were averaged over different 3 scanned samples of size approx. 2 $\times$ 1 mm^2. Fig. 3(a) and (b) show the probability density distributions of the azimuthal, ϕ, and polar angles, θ, respectively, that are representative of the in-plane and through-plane orientation of the identified individual fiber branches. The angles are calculated as $\phi = \arctan\left(\frac{y_2-y_1}{x_2-x_1}\right)$ and $\theta = \arccos\left(\frac{z_2-z_1}{|\vec{r}_2-\vec{r}_1|}\right)$. The figures indicate that fibers are practically orientated at random in the in-plane direction (xy-plane) for the particular case of Toray paper, while they follow a particular narrow distribution in the through-plane direction with a mean value $\theta \approx \pi/2$, that exactly coincides with the direction parallel to the paper surface. It should be noted that the uniformly random fiber orientation in the xy-plane direction is an intrisic feature of Toray papers, while papers by other manufacturers also exhibit anisotropy in all three directions [6].

This type of anisotropy is quite satisfactorily described by the polar angle distribution density function proposed by Schladitz et al. [23], which is also used in our study. For the spatial distribution of the resin over the fibrous skeleton, we propose however a novel process-based stochastic reconstruction algorithm that pursues the minimization of the interfacial energy of the system based on the simulated annealing method of Kirkpatrick et al. [25]. This approach can be considered as a proper superset of the morphological opening algorithm, as physically meaningful resin distributions can be realized, including different resin-fiber contact angles and the formation of wetting films for a perfectly wetting resin phase. The transport properties of the produced fiber-resin composites are then calculated using a series of state-of-the-art numerical models that describe transport phenomena at the microscale to capture the effects of anisotropy and resin content.

3. Stochastic reconstruction of the C-fiber composite

In this section we present the stochastic reconstruction methodology that will be used in the following sections for the determination of the material transport properties. As discussed in the previous section, the material is a carbon-carbon composite, that consists of initially carbonized PAN fibers and is impregnated with a carbonizable resin. The composite is then graphitized to enhance its structural and transport properties.

The composite structure of the carbon fabric impregnated with resin was digitally reconstructed based on a stochastic methodology that consists of two steps; the construction of the fibrous skeleton, made of overlapping cylindrical segments of fixed radius, corresponding to the initial fibrous matrix, followed by the spatial distribution of the resin material in a thermodynamically consistent fashion, pursuing the minimization of the interfacial energy of the void, fibrous and resin system.

3.1. Reconstruction of the fibrous skeleton

The digital reconstruction of the fibrous skeleton, prior to resin impregnation, is realized following the standard method of Schladitz et al. [23]. According to this method overlapping cylindrical segments are deposited in 3D space, with the projection of their principal axis randomly distributed in the xy-plane (azimuthal angle, ϕ), while the polar angle, θ (z-direction) obeys the following probability density function;

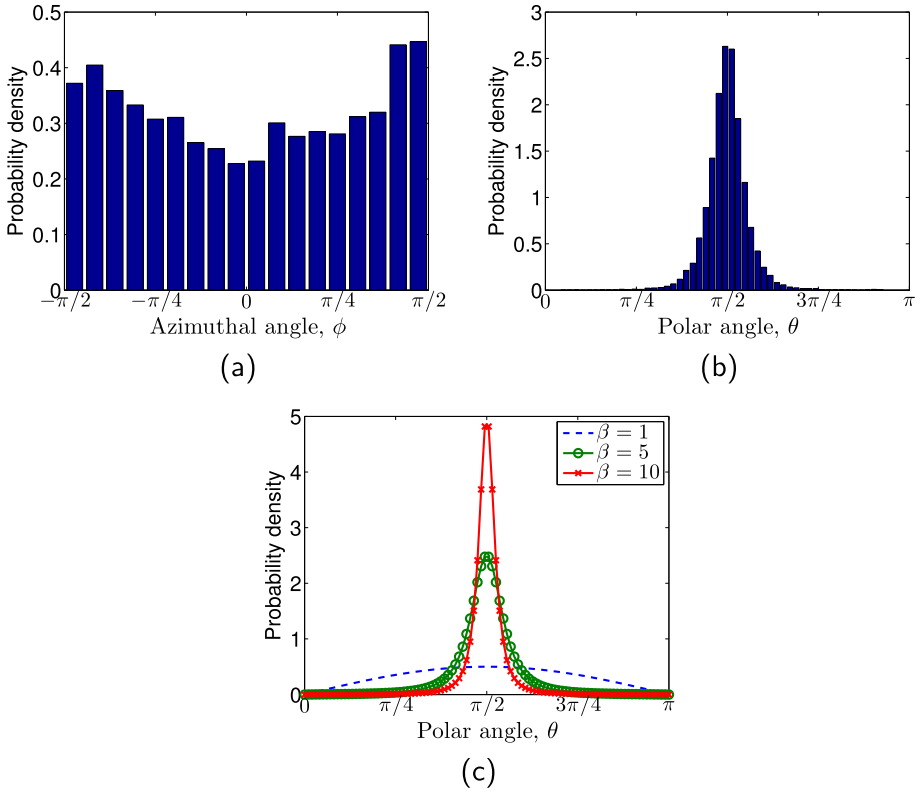

Fig. 3. Experimentally determined orientation of carbon fiber segments in 3 samples of Toray 090 paper. (a) Probability density of azimuthal angle, ϕ, (angle from the x-axis of fiber projection on the x-y plane). (b) Probability density of polar angle (angle of the fiber with the z-axis). The results are averaged over 3 scanned samples from the same Toray sheet. Also shown in (c) is the theoretical probability distribution of the polar angle, θ, for different values of the parameter β using Eq. (1).

$$p_z(\theta) = \frac{1}{2}\frac{\beta \sin\theta}{\left(1+\left(\beta^2-1\right)\cos^2\theta\right)^{3/2}} \tag{1}$$

Similarly, the probability distribution in the xy-plane can be expressed as $p_{xy}(\phi)=1/2\pi$, and the overall probability as $p(\theta,\phi) = p_z(\theta)p_{xy}(\phi)$. The parameter β controls the anisotropy of the medium by adjusting the variance of the above density distribution function for the polar angle.

Fig. 3(c) shows the probability density distribution for different values of β obtained with Eq. (1), which compares well with the experimentally determined polar angle probability density distribution of Fig. 3(b) for a value of $5 \leq \beta \leq 10$. We should note however that this particular mode of calculation of the polar angle should be only viewed as a draft indicator of the medium anisotropy, as several branches identified by ImageJ may belong to the same single fiber.

In our simulations, we add cylinders with a fixed diameter $d = 7\delta x$ in 3D digital domains of size $512^3\delta x^3$, assuming a spatial resolution of 1 μm = 1 δx, until the desired porosity for the fibrous skeleton (prion to resin deposition), ε_0, is reached. The principal axis of each cylinder is characterized by a set of angles (θ,ϕ) that follow the above mentioned probability distributions and a position vector $\vec{x}$ selected at random in the discrete 3D domain. The produced binary domain space can be then described by the phase function $\mathcal{Z}(\vec{x})$, defined as;

$$\mathcal{Z}(\vec{x}) = \begin{cases} 1 & \text{if } \vec{x} \text{ belongs to the pore space (void)} \\ 0 & \text{otherwise (solid)} \end{cases}, \tag{2}$$

where $\vec{x}$ is the position vector of the voxel center from an arbitrary origin. The porosity, ε_0, can be defined by:

$$\varepsilon_0 = \langle \mathcal{Z}(\vec{x}) \rangle. \tag{3}$$

For completeness, we provide in Appendix A a detailed description of the fiber deposition algorithm used in this study. Fig. 4(a) and (b) show a series of such reconstructed fibrous skeletons for two different values of the anisotropy parameter, β. It is evident that the fibers become increasingly aligned in the xy-plane for higher values of β.

3.2. Simulation of the resin impregnation

We further assume that the resin binder is deposited over the original fibrous skeleton taking into account that its spatial distribution mimics that of a wetting fluid in the pore space within the previously constructed network of cylindrical segments. In our approach, we implement a numerical model that pursues the minimization of the interfacial area of the fiber, resin and void phases, by appropriately redistributing in space void and resin voxels, thus arriving to thermodynamically consistent spatial distributions, unlike other previously proposed methods that relied on morphological and phenomenological approaches [21,22].

Starting from the original fibrous skeleton with porosity ε_0, that contains only solid, $\mathcal{Z}(\vec{x}) = 0$, and void voxels, $\mathcal{Z}(\vec{x}) = 1$, a set of random void voxels, equal to $(\varepsilon_0 - \varepsilon)L^3$, are converted to resin voxels in order to achieve the final porosity of the composite, ε. Initially, these voxels are denoted by $\mathcal{Z}(\vec{x}) = 2$. Assuming that the bulk phase density of both composite components (fibers and resin) is practically equal after graphitization, it is straightfoward to express the porosity of the fibrous skeleton, ε_0, as a function of the final porosity, ε, of the composite (after resin deposition) and the

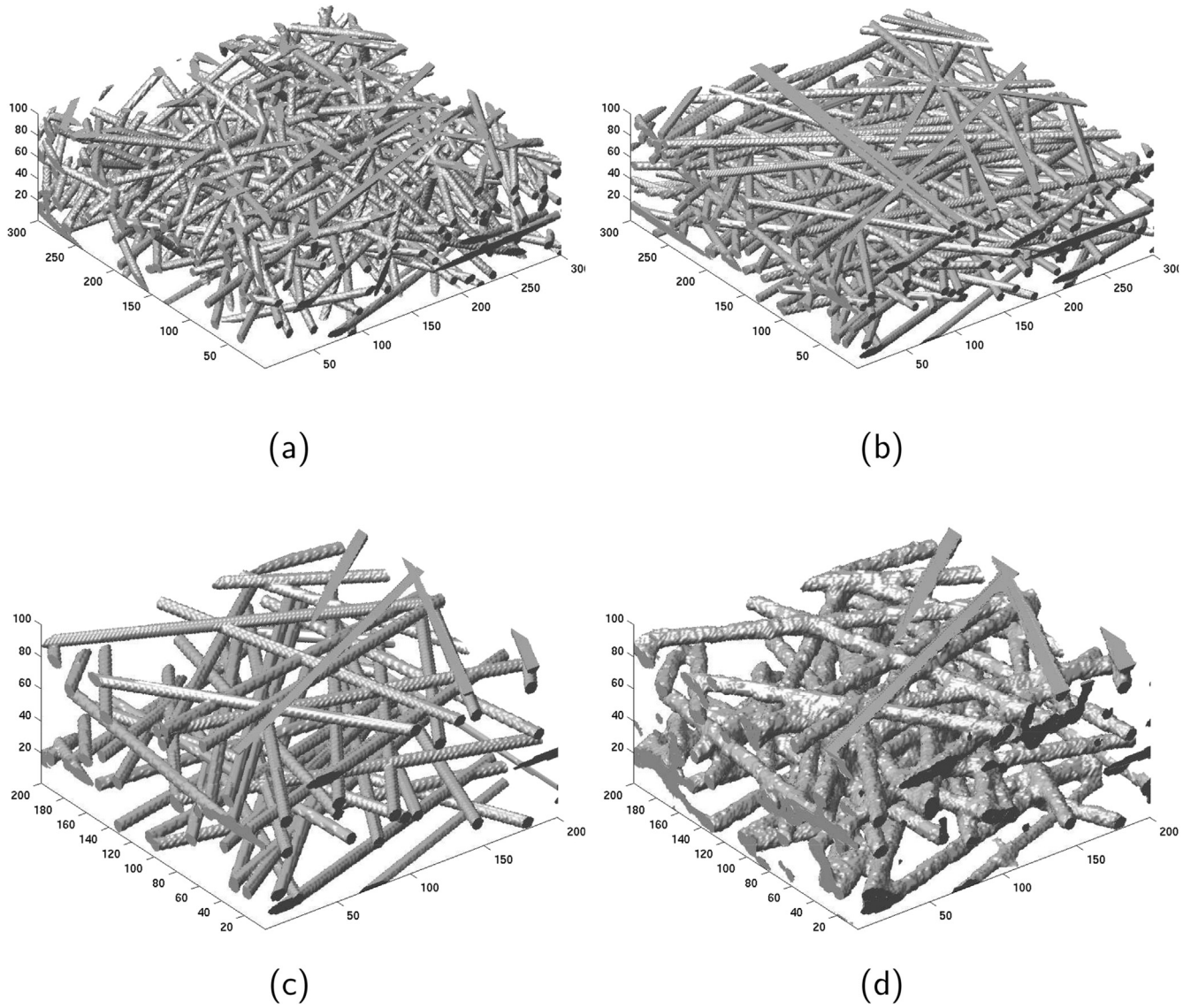

Fig. 4. Stochastically reconstructed fiber skeletons prior to resing impregnation for (a) $\beta = 2$ and (b) $\beta = 100$, and an initial porosity, $\varepsilon_0 = 0.84$. Also shown is a detail of a digital domain with $\beta = 100$ (c) before and (d) after resin deposition with the Simulated Annealing method of this study. Resin mass fraction $\chi = 0.5$ and final porosity $\varepsilon = 0.8$.

desired resin content, $\chi \in [0,1]$, as;

$$\varepsilon = \frac{\varepsilon_0 - \chi}{1 - \chi}. \tag{4}$$

In order to calculate the total "interfacial area" of the produced phase distribution, we set a fictitious interfacial interaction, $\gamma(\alpha,\beta)$ for each pair of phases α and β according to Young's equation:

$$\gamma(1,2) = \gamma(0,1) - \gamma(0,2) \tag{5}$$

where the index 0 corresponds to the solid phase (fiber skeleton), 1 to the void phase and 2 to the resin phase, which is initially randomly distributed. The values for the interactions in this study are $\gamma(0,1) = 30$, $\gamma(0,2) = 25$ and consequently $\gamma(1,2) = 5$ in arbitrary units of energy per unit area. Additionally, $\gamma(\alpha,\beta) = \gamma(\beta,\alpha)$ and $\gamma(\alpha,\alpha) = 0$.

The total interfacial energy, G_s, of the produced phase distribution is then a functional of $\mathcal{Z}(\vec{x})$ and can be derived as follows;

$$G_s\{\mathcal{Z}(\vec{x})\} = \frac{1}{2}\sum_i \sum_j A\gamma\left(\mathcal{Z}(\vec{x}_i), \mathcal{Z}(\vec{x}_j)\right), \tag{6}$$

where $A = \delta x^2$ is the elementary interfacial area, i spans over every voxel and j spans over nearest neighbors of i.

In order to determine the function $\mathcal{Z}(\vec{x})$ that corresponds to the minimum of G_s for the spatial distribution of the resin voxels, we employ the method of simulated annealing (SA), introduced by Kirkpatrick et al. for the minimization of multidimensional functions [25]. As stated previously, a specific number of phase-1 (void) voxels, in random positions are initially marked as phase-2 (resin). Then a pair of phase-1 and phase-2 voxels are selected at random and exchange their positions. This swap results in a variation of the interfacial energy G_s by ΔG_s. If $\Delta G_s \leq 0$, then the new configuration is unconditionally accepted, while if $\Delta G_s > 0$, the new configuration is accepted with a probability given by;

$$P = \exp\left(-\frac{\Delta G_s}{G_{ref}^{(n)}} \right), \tag{7}$$

where $G_{ref}^{(n)}$ is an analog of the k_BT parameter in the Metropolis algorithm, k_B is the Boltzmann constant and T is the ambient temperature. This conditional acceptance of phase distributions that have higher interfacial energies than the previous one allows for exploring the entire solution space in order to avoid configurations corresponding to local energy minima.

After a sufficient number of iterations ($\approx 10^7$ new states for a fixed value of G_{ref}), the system approaches an equilibrium state, where the value of G_s remains practically constant. We then gradually decrease the reference energy state to $G_{ref}^{(n+1)} = \lambda G_{ref}^{(n)}$ where $\lambda < 1$, and repeate the simulation process starting from the previously determined equilibrium configuration. The parameter λ characterizes the so called 'cooling schedule' and is set equal to 0.99 in our simulations. In this way, it is possible to achieve progressively new lower energy levels of G_s towards a global energy minimum. The process is considered complete when despite the change in G_{ref}, the number of accepted interchanges becomes lower than a predefined value (in our case when the ratio of the number of accepted interchanges to the total number of trials becomes lower than 10^{-5}). As a final step, all phase-2 voxels are converted to phase-0, and the phase function corresponding to the minimum G_s for the specific porosity is achieved. It must be noted that since we search for the function $Z(\vec{x})$ that corresponds to the minimum G_s, the final configuration is independent of the selected $\gamma(\alpha,\beta)$ values, provided that these satisfy Eq. (5). The parameters values selected for our study are obtained by trial and error tests in order to optimize the required computational time.

Fig. 4(c) shows the an initial fibrous skeleton with porosity $\varepsilon_0 = 0.9$ prior to resin deposition and the resulting structure of the composite material (fibrous skeleton + resin) with porosity $\varepsilon = 0.8$ (Fig. 4(d)) after application of the previously described SA algorithm. This particular configuration corresponds to the minimum interfacial energy for the fiber, resin and void phases, given the fixed position of the fibrous skeleton. As seen in this figure, resin is deposited primarily at the intersections and small pores between fibers, thus increasing the effective intersectional area (contact area between intersecting fibrous segments), while at the same time it forms a film that covers the external surfaces of the fibers, thus slightly increasing their apparent diameter. We should note here that the formation of resin films is consistent with a perfectly wetting resin phase, while different contact angles can be realized by appropriately adjusting the resin-fiber-void interfacial tensions of Eq. (5). We expect however that the effects of this slight increase of fiber radii on the medium transport properties are negligible compared to the effects of resin accumulation at fiber intersections, and thus assume perfect wetting for the reconstruction of our media. These effects will be studied in detail in the following sections.

4. Microscale modeling of transport properties

For the determination of the transport properties of the stochastically reconstructed domains of the composite fibrous material, we employ a series of state-of-the-art pore scale numerical models that rigorously recover conservation equations in the complicated geometry of both the solid and void domains. In the following section, we discuss these numerical models that are applied for the calculation of Darcy permeabilities and diffusivities in the void space, and thermal and electrical conductivities in the solid domains, in both spatial directions.

4.1. Darcy permeability

For the solution of the velocity profile in the void space of the stochastically reconstructed, as well as the digital μ-CT domains, we employ a Lattice-Boltzmann (LB) model that recovers the solution of the incompressible Navier-Stokes and continuity equations in the limit where Re $\rightarrow$ 0 [26]. Fluid mass and momentum densities are described at the mesoscale (below the scale where the 'continuum' hypothesis is valid) through a particle distribution function, $f(\vec{x},t)$, where $\vec{x}$ is the position vector in the fluid space and t is time. The particle distribution function is selected so that it is satisfies a Maxwell-Boltzmann probability distribution for particle velocities at thermodynamic equilibrium, $f(\vec{u})$, where $\vec{u} = \vec{u}(\vec{x}) = (u_x, u_y, u_z)$ is the local macroscopic velocity (at the scale where the 'continuum' hypothesis is valid). We provide in Appendix B the basic LB algorithm used for this study for the calculation of the velocity profile.

The volume-averaged Darcy-scale velocities are then calculated as;

$$\left\langle u_i \right\rangle = \frac{\int_V u_i dV}{\int_V dV} \tag{8}$$

where $i = x,y,z$ and the permeabilities are determined from Darcy's law given the applied body force (or pressure gradient), $\vec{G} = \nabla p/\rho = (g_x, g_y, g_z)$, used to generate flow and the kinetic fluid viscosity, ν_0, and density of the fluid, ρ, as follows;

$$K_{\parallel} = \frac{K_x + K_y}{2} = \frac{\nu_0}{2}\left(\frac{\langle u_x \rangle}{g_x} + \frac{\langle u_y \rangle}{g_y} \right) \quad \text{and} \quad K_{\perp} = K_z = \frac{\langle u_z \rangle \nu_0}{g_z} \tag{9}$$

Fig. 5(a) shows a typical pore scale velocity magnitude profile calculated using the above LB model in a stochastically reconstructed domain (Fig. 5(b)) with $\varepsilon = 0.8$, $\chi = 0.2$ and $\beta = 10^2$. Similar results are obtained for the pore scale velocity calculated with LB for a small subdomain of the X-ray μ-CT sample, as shown in Fig. 5(c)-(d). Despite their stochastic nature, the two domains exhibit remarkably similar pore scale characteristics, e.g. fibrous diameter, anisotropy, spatial resin distribution, even at length scales of a few tens of microns.

4.2. Effective diffusivity, thermal and electrical conductivities

The effective diffusivity and conductivity of the binary domains are calculated using a 'blind' random walk algorihm [27]. This method is based on monitoring the random movement of a population of particles (e.g. molecules, electrons etc.), otherwise called 'random-walkers', as they travel within a heterogeneous structure that consists of conductive and non-conductive spatial regions. Each 'random-walker' is initially placed at a random position in space, corresponding to a discrete voxel that could either belong to the conductive phase (phase-C) or the insulator (phase-I). If the voxel belongs to phase-C, the trajectory of the walker is monitored vs time, while in the opposite case the walker remains stationary over the entire process. At every time step δt a random trial move of length δx towards one of the six neighboring pixels is attempted (on-lattice). Assuming that the conductivity of the bulk phase-C is equal to σ_0, the time step δt is selected to satisfy the condition $\delta x^2 = 6\sigma_0 \delta t$. The new position then is unconditionally accepted for moves between neighboring phase-C voxels, while moves towards phase-I voxels are rejected, resulting in zero particle displacement during the particular time step.

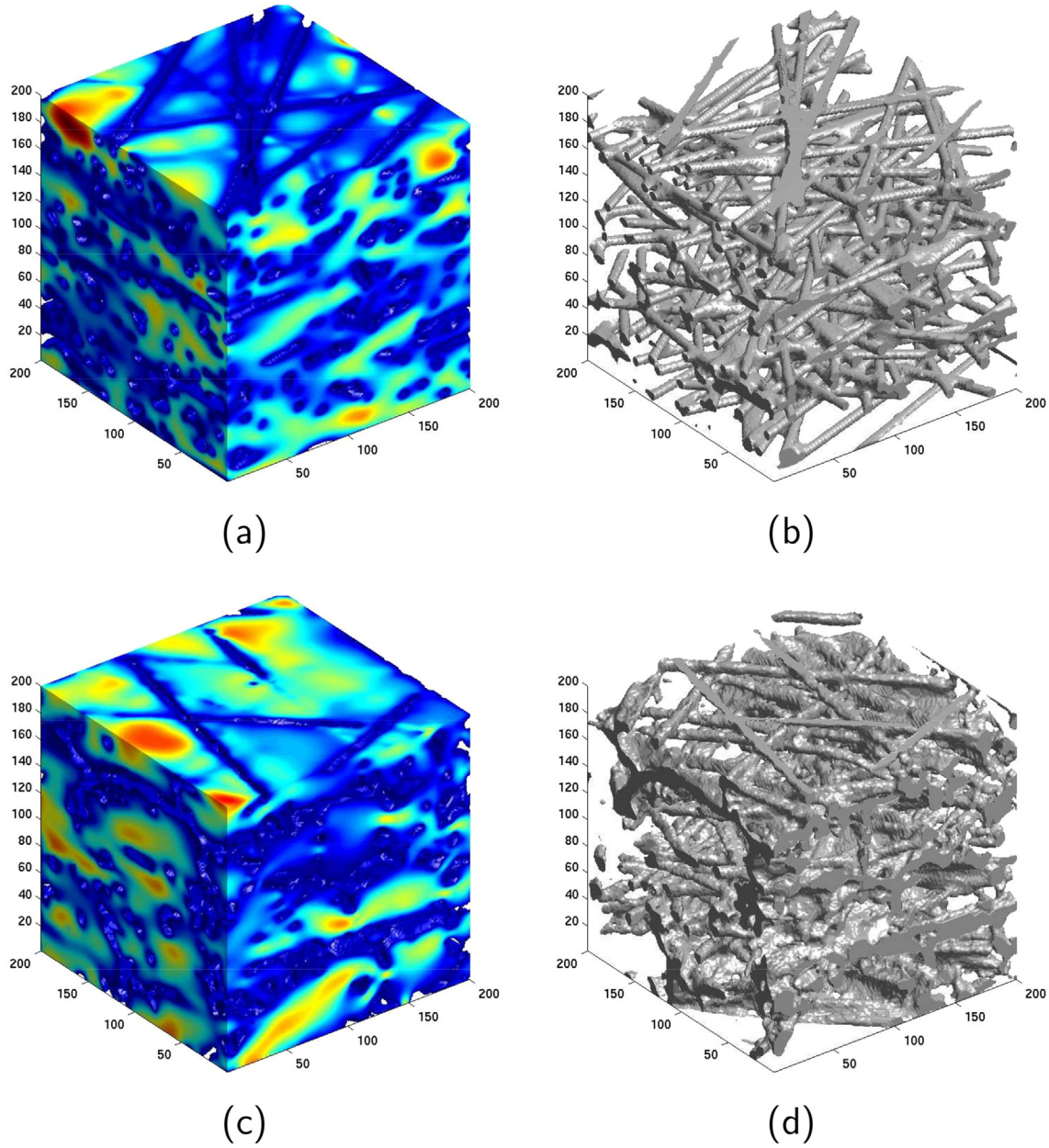

Fig. 5. (a) Velocity magnitude profiles from LB simulations in a reconstructed digital domain (b) of size 200 x 200μm^3 ($\beta = 100$, $\chi = 0.2$ and $\varepsilon = 0.8$), and (c) in an X-ray μ-CT domain (d) with $\varepsilon = 0.78$ of the same size.

The procedure is repeated for a sufficiently large number of time steps and the effective conductivities of the heterogeneous domain, $\sigma_{\parallel}$ and $\sigma_{\perp}$, are computed as a function of the bulk phase conductivity, σ_0, using Einstein's relation;

$$\sigma_{\parallel} = \lim_{t\to\infty} \frac{\langle x^2(t) + y^2(t)\rangle}{4t}, \tag{10}$$

$$\sigma_{\perp} = \lim_{t\to\infty} \frac{\langle z^2(t)\rangle}{2t}, \tag{11}$$

where $\langle x^2(t)\rangle$, $\langle y^2(t)\rangle$ and $\langle z^2(t)\rangle$ are the mean square displacements of a statistically sufficient number of random-walkers at time t, and at $x-$, $y-$, $z-$ directions respectively. In non-dimensional form:

$$\frac{\sigma_{\parallel}}{\sigma_0} = \frac{3}{2} \lim_{n\to\infty} \frac{\langle X^2(n) + Y^2(n)\rangle}{n_t}, \tag{12}$$

$$\frac{\sigma_{\perp}}{\sigma_0} = 3 \lim_{n\to\infty} \frac{\langle Z^2(n)\rangle}{n_t}, \tag{13}$$

where $n_t = t/\delta t$ and $X(n_t) = x(n_t\delta t)/\delta x$, $Y(n_t) = y(n_t\delta t)/\delta x$. $Z(n_t) = z(n_t\delta t)/\delta x$. We should note that all 'random-walkers', including those that are initially placed at voxels of zero conductivity, are accounted for in the calculation of the mean square displacements.

This method will be applied both for the calculation of effective diffusivities of the composite (by setting the void space as the conductive phase and the solid skeleton as the insulator), but also calculating the thermal/electrical conductivities of the solid

structure (resin + fibrous skeleton) by considering the latter as the conductive phase, while the void phase is an insulator.

5. Results and discussion

We performed a series of numerical simulations combining the previously described methods in order to determine the transport and structural properties of both the stochastically reconstructed media, as a function of porosity, anisotropy and resin content, but also the properties of the binarized domains obtained using X-ray μ-CT imaging. For the stochastically reconstructed structures, all simulations were performed on $512^3\delta x^3$ domains assuming a spatial resolution of $\delta x = 1\mu m$ and a fixed fiber radius equal to $R = 3.5\delta x$. In order to verify that the calculated values were insensitive to the selected resolution, we have also performed a series of simulations on larger domains of size $1024^3\delta x^3$ (setting the fiber radius to $R = 7\delta x = 3.5\mu m$, thus $\delta x = 0.5\mu m$), resulting however in practically identical results.

5.1. Effects of porosity, anisotropy and binder content on hydraulic permeability

Lattice Boltzman simulations were performed using a body force density, $G = 10^{-8}\ \rho\delta x/\delta t^2$, to drive the flow assuming a Newtonian fluid with kinematic viscosity $\nu_0 = \frac{1}{6}\delta x^2/\delta t$, corresponding to a relaxation time $\tau_0 = 1$, and a reference density ρ taken equal to unity for simplicity, thus leading to Reynolds numbers $Re \ll 1$. The effects of the selected value for the relaxation parameter, τ_0, on the calculated permeabilities were also systematically investigated and were found negligible for the particular spatial resolution [28].

Fig. 6(a) and (b) show the in-plane and through-plane Darcy permeabilities, denoted as $K_\parallel$ and $K_\perp$, respectively, of the fibrous skeleton prior to resin deposition (thus for $\chi = 0$) as a function of the material porosity and for different values of the anisotropy parameter β. The reported results are averages over 5 different fibrous domains with the same β, ε and χ values, and the standard deviation of the entire data set is less than 3%. As expected, the in-plane and through-plane values are found to be equal for the isotropic case ($\beta = 1$) over the entire range of porosities of this study. As the medium anisotropy is varied by adjusting the value of β, both permeabilities change, but in the opposite direction. The most important effect is observed on through-plane values, where for increasing β values, namely for fibers progressively more aligned in the xy-plane, $K_\perp$ can be up to 30% lower than the isotropic case value. Apparently, the orientation of the fibers in the direction normal to flow significantly hinders flow, leading thus to decreased permeabilities. The in-plane permeability however appears to increase only slightly (up to 5%) for larger values of β compared to the isotropic case.

These results, in the absence of resin, can be compared with the theoretical predictions of Tomadakis and Robertson who proposed the following formula for randomly overlapping fiber structures, either randomly oriented in space, or aligned in the xy-plane [29];

$$\frac{K}{R^2} = \frac{\varepsilon}{8\ln^2\varepsilon}\frac{\left(\varepsilon-\varepsilon_p\right)^{\alpha+2}}{\left(1-\varepsilon_p\right)^{a}\left[(a+1)\varepsilon-\varepsilon_p\right]^2} \tag{14}$$

where the parameters a and ε_p depend on the direction of the flow and the anisotropy of the structure. Fig. 6(a)-(b) thus also show the predictions of the above equation for $K_\parallel$ and $K_\perp$ for the isotropic case, denoted as 3D, and for the extreme limit where the fibers are oriented in the xy-plane only, denoted as 2D. The latter case corresponds to a fibrous skeleton constructed in our study with $\beta \to \infty$.

The theoretical curves compare quite well with our numerical results, for both the isotropic case ($\beta = 1$ compared to the Tomadakis 3D solution) and the extreme anisotropic limit, where the fibers are aligned in the xy-plane ($\beta = 10^2$ compared to the Tomadakis 2D solution). Furthermore, these theoretical solutions predict similar trends with our results, regarding the dependance of the permeabilities on the structure anisotropy, with a 25% decrease of $K_\perp$, as we increase anisotropy (from the 3D to the 2D solution limit), and a 5% increase of $K_\parallel$ for the same structural changes.

These effects are also illustrated in the inset of Fig. 6(b) that shows the ratio of $K_\parallel/K_\perp$ for the theoretical 2D limit and our numerical results for different β values. The permeability ratio changes from unity in the isotropic case ($\beta = 1$) to progressively larger values, as β increases towards the asymptotic limit of the theoretical predition of Tomadakis for the 2D case. It is worth noting that the in-plane values are always higher (up to 50%) compared to the corresponding through-plane ones, resulting in the required enhanced flow of the reacting species below the ribs of the bipolar plane in GDLs.

In a next step we studied the effects of resin deposition on top of the fibrous skeleton on the permeabilities of the reconstructed structures. Fig. 6(c) and (d) show both $K_\parallel$ and $K_\perp$ for 20% resin content ($\chi = 0.2$) and different values of β. Also shown in these figures are the theoretical predictions of Tomadakis and Robertson [29] for the extreme 2D limit for two values of the fiber radius. While qualitatively similar to the permeabilities of the plain fibrous skeleton (and with similar trends with respect to the effects of anisotropy through β), the actual values for $\beta = 10^2$ no longer compare so well with the theoretical predictions of the 2D case for $R = 3.5\ \mu m$. In fact, the calculated permeabilities with 20% resin are typically higher than those of the plain fibrous skeleton without resin, and they lie in a region defined by the theoretical predictions of Tomadakis for $R = 3.5\ \mu m$ and a somehow larger radius equal to $R = 5.0\ \mu m$. This result should be primarily attributed to the effect of the reduced fiber number density (number of unique fibers of radius $R = 3.5\mu m$ per unit volume of the 3D domain) in the structures with resin compared with those of the plain fibrous skeleton for the same porosity. Note that for $\chi = 0$, the final porosity is equal to that of the fibrous skeleton, namely $\varepsilon = \varepsilon_0$, while for structures with resin, $\chi > 0$, the final porosity is always lower $\varepsilon < \varepsilon_0$. This leads to the formation of a less dense fibrous matrix for $\chi > 0$ with fewer fiber intersections and thus higher permeabilities for the same porosities.

As shown in Fig. 6(c) and (d), the calculated permeabilities actually correspond to structures with higher fibrous radii (than the initially used $R = 3.5\ \mu m$ to generate the fibrous skeleton) in the range of $3.5\ \mu m < R \leq 5.0\ \mu m$. This is also due to the resin deposition algorithm (simulated annealing) that aims to reduce to void-solid interfacial area in favor of the resin-void area. Resin deposition occurs primarily on the walls and intersections of the fibrous skeleton (as should be expected for a wetting fluid), thus increasing the average apparent radius of the fibers (see also Fig. 4(c)-(d)). The above effects are also demonstrated in Fig. 6(e) and (f) that show the corresponding calculated permeabilities for a high degree of anisotropy ($\beta = 10^2$) and for different resin contents, χ.

5.2. Effective diffusivity and tortuosity of the medium

Following the above permeability calculations, we proceed to characterise the material in terms of its effective diffusivity, which is expected to be the dominant mass transport mechanism for all species in the through-plane direction. We performed a series of random-walk simulations with the algorithm described previously, taking void as the conductive phase. Our implementation of the random-walk algorihm is an on-lattice variant where a total of

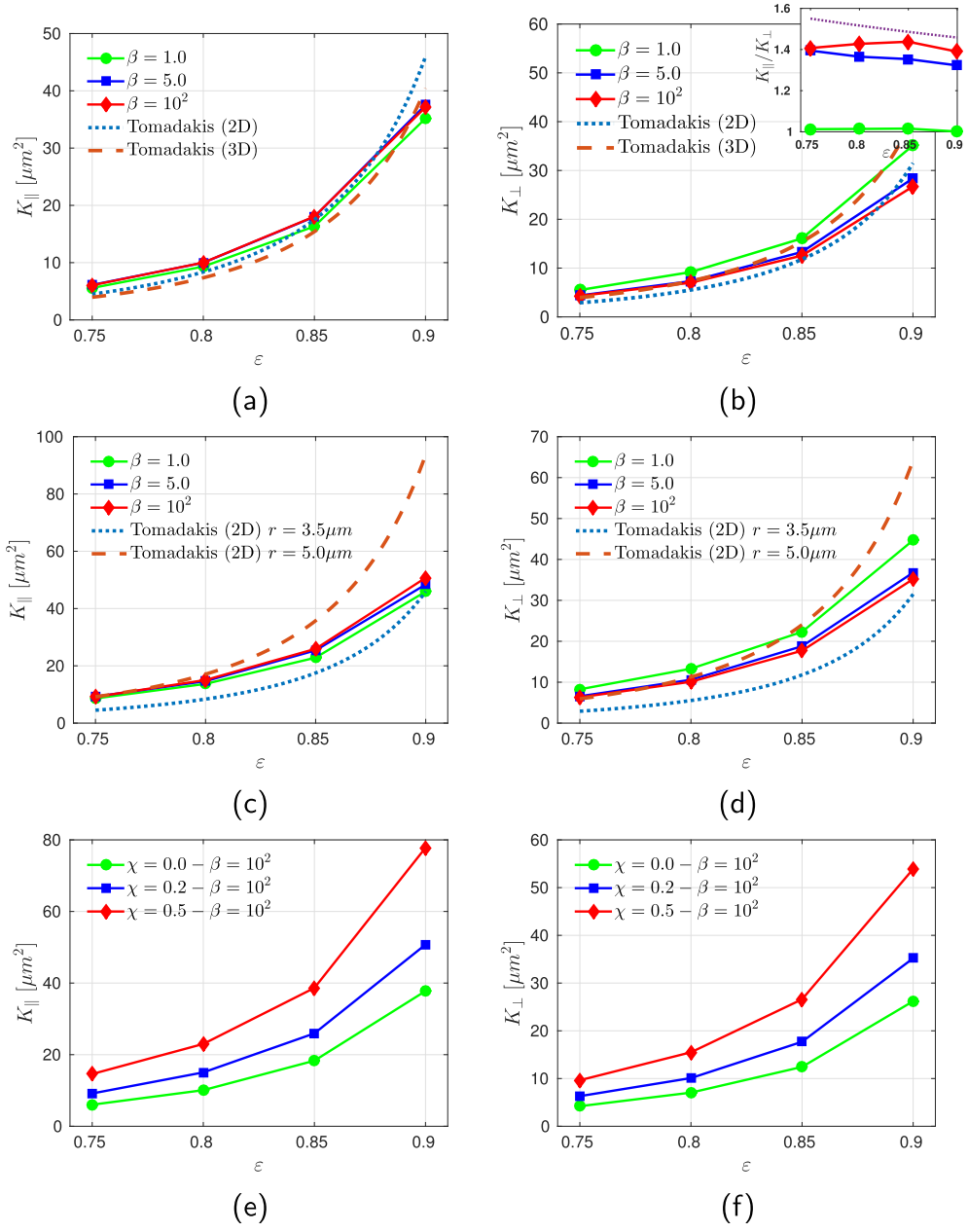

Fig. 6. (a) and (b) Calculated in-plane and through-plane permeabilities of the fiber skeleton (prior to resin deposition, thus $\chi = 0$) as a function of porosity, ε, and for different values of the anisotropy parameter, β. The values are averaged over 5 different fibrous domains and the maximum error for the entire data set is less than 3%. (c)-(d) Permeabilities of the composite material (fibers + resin) for $\chi = 0.2$ resin content. (e)–(f) Permeabilities of the composite material (fibers + resin) for different values of the resin content, χ, and a high value of the anisotropy parameter, $\beta = 10^2$. Also shown are the theoretical curves of Tomadakis and Robertson [29] for an isotropic fiber skeleton, denoted as the 3D case, and for an anisotropic fiber skeleton where fibers are aligned in the xy-plane only, denoted as the 2D case.

$n_p = 6 \times 10^5/\varepsilon$ random-walkers are placed at random in space and they are allowed to move in one of the six predefined neighboring voxels. If a particle is placed in a solid voxel (corresponding to either fiber or resin), it remains immobile over the entire process (insulating phase). A total of $n_t = 2 \times 10^5$ random moves take place, corresponding to the simultaneous displacement of all molecules at random nearest-neighboring voxels, and the mean square displacement of the entire population in all 3 spatial directions with respect to the origin of each particle is calculated, including the immobile walkers. The above values for parameters n_p and n_t have been selected so that both a representative part of the void space is covered by the random walkers, n_p, but also the 'walkers' are allowed enough time steps, n_t, to cover at least once the entire domain. Using thus Eqs.(12) and (13), we calculate the so-called formation factor F of the material, that is a function of its porosity, ε, and tortuosity, τ as follows;

$$\frac{D_\parallel}{D_0} = F_\parallel = \frac{\varepsilon}{\tau_\parallel} \quad \text{and} \quad \frac{D_\perp}{D_0} = F_\perp = \frac{\varepsilon}{\tau_\perp} \tag{15}$$

where $D_\parallel$ and $D_\perp$ are the in-plane and through-plane effective diffusivities, respectively, D_0 is the bulk (void) phase molecular diffusivity (namely, for a material with $\varepsilon = 1$), and $\tau_\parallel$, $\tau_\perp$ are the in-plane and through-plane tortuosities, respectively.

Fig. 7(a) and (b) show the calculated in-plane and through-plane formation factors, respectively, for the effective diffusivity of a

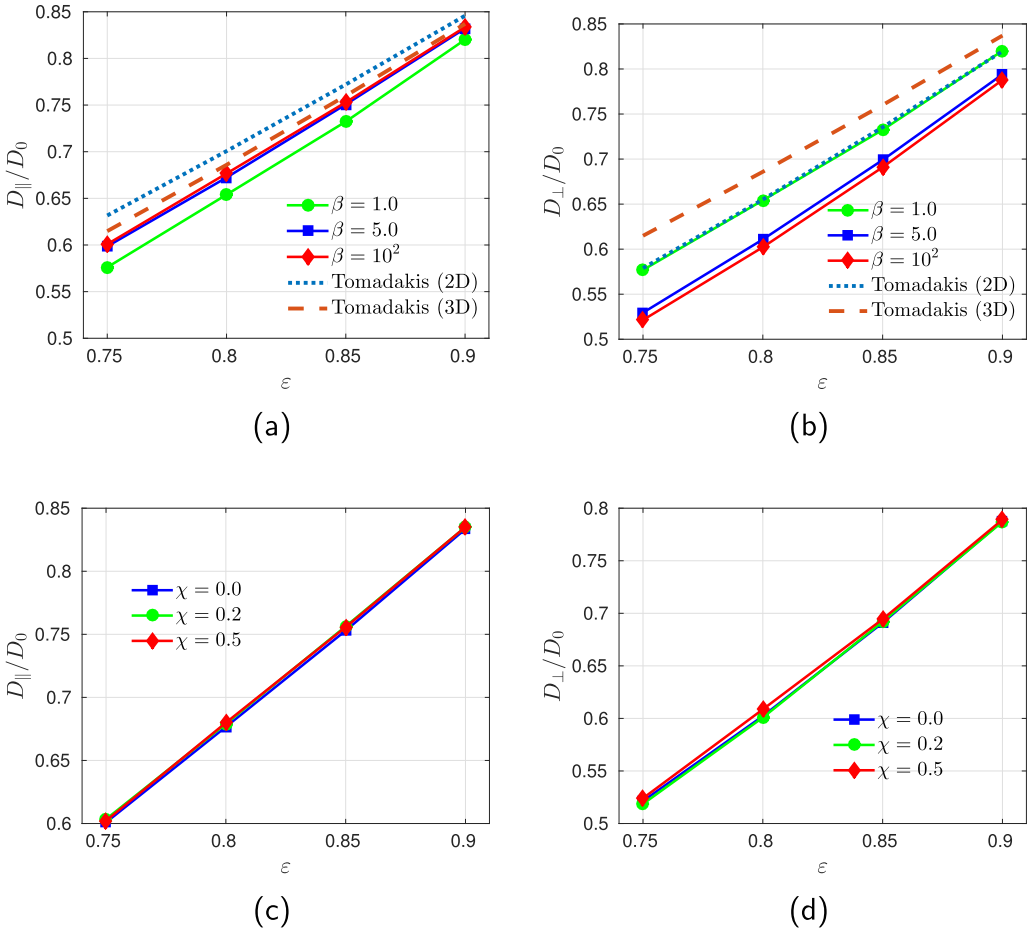

Fig. 7. (a) and (b) Calculated in-plane and through-plane effective diffusivities of the fiber skeleton (prior to resin deposition, thus $\chi = 0$) as a function of porosity, ε, and for different values of the anisotropy parameter, β. The values are averaged over 4 different fibrous domains and the maximum error for the entire data set is less than 0.4%. (c)-(d) Effective diffusivities of the composite material (fibers + resin) for different values of the resin content, χ, and for a high value of the anisotropy parameter, β=10^2. Also shown are the numerical results of Tomadakis and Robertson [29] for an isotropic fiber skeleton, denoted as the 3D case, and for an anisotropic fiber skeleton, where fibers are aligned in the xy-plane only, denoted as the 2D case.

fibrous domain prior to resin deposition, as a function of porosity for different values of the anisotropy parameter, β. The reported results are averages over 4 different fibrous domains with similar β, ε and χ values, and the standard deviation of the entire data set is less than 0.4%. As expected, the calculated values of $D_{\parallel}$ and $D_{\perp}$ are equal for the isotropic case ($\beta = 1$) over the entire range of porosities. However, as the anisotropy of the medium increases (for higher β values), the in-plane diffusivities also increase (although quite slightly, in the order of less than 3%), while their through-plane counter-parts exhibit a more pronounced decrease in the order of 10%. These results are qualitatively similar to those calculated in the previous section for the medium permeabilities, and should be also attributed to the increasing orientation of the fibers in the xy-direction, that enhances flow and mass transfer in this direction, at the cost, however, of poorer through-plane transport properties.

Tomadakis and Sotirchos [30] also calculated numerically the effective diffusivities in fibrous domains (but in the absence of resin) for the isotropic case (3D fiber orientation) and for the extreme case where the fibers are aligned in the xy-plane (2D fiber orientation). They used an off-lattice random-walk algorithm in domains quite smaller than those of our study to propose a generalization of Archie's formula in fibrous structures, as follows;

$$\frac{D_e}{D_0} = \frac{\varepsilon}{\tau} = \varepsilon\left(\frac{1-\varepsilon_p}{\varepsilon-\varepsilon_p}\right)^{-a} \tag{16}$$

where D_e is the effective diffusivity, ε_p is the percolation threshold is each direction and α is an exponent, that both depend on the orientation of the fibers and the direction under consideration. They used a least-square fit in order to calculate the values of parameter, α, for both the 2D and 3D cases.

Fig. 7(a) and (b) also show the results of Tomadakis and Sotirchos [30] for $D_{\parallel}/D_0$ (left) and $D_{\perp}/D_0$ (right) for the isotropic and extreme anisotropic cases. Their results for the in-plane diffusivities compare quite favorably with our predictions, exhibiting also similar trends, namely, the in-plane diffusivity increases for increasing medium anisotropy. A less satisfactory agreement (with a typical 8–10% overestimation by the Tomadakis and Sotirchos formula) is observed for the through-plane values, while the trends for increasing anisotropy remain however similar in both datasets. These slight differences could be due to the smaller size of the computational domain of Tomadakis and Sotirchos, as well as the different type of boundary conditions utilized in their study (specular reflexion compared to periodic boundaries in our simulations).

Finally, Fig. 7(c) and (d) show the effects of resin content on the diffusivities for a relatively high value of the anisotropy parameter,

$\beta = 10^2$. It is evident from these simulations that there is a practically negligible effect of χ, even for values as high as 50%, unlike the significant effect of resin content on medium permeabilities that was demonstrated in the previous section (i.e. Fig. 6(e) and (f)).

5.3. Thermal and electrical conductivities

In a similar fashion as above, we have calculated the thermal and electrical conductivities of the fibrous-resin composite. Using the random-walk method, a total number of $n_p = 10^5/(1-\varepsilon)$ random-walkers were randomly distributed in space. This time, however, the particles originally located in the void space were taken immobile (insulator), while the particles that landed on either the fibrous or resin space were allowed to move at random in the 6 neighboring voxels for a total $n_t = 10^6$ displacements (conductor). Note that a different set of values for parameters, n_p and n_t, are selected (compared to the values used for the diffusivity calculations) in order to account for the different characteristics of the solid domain (i.e. smaller phase fraction and poorer conductivity).

The mean square displacement in each direction is again calculated over the total population of particles (including immobile particles at void voxels) and the effective conductivities of the material are estimated using Eqs.(12) and (13). The main assumption of our study is that the transport properties of both components of the composite, either resin or the fibrous skeleton, are practically the same after the graphitization process (the final step of C-fiber paper production process, as described by Mathias et al. [2]). This allows for considering the solid as a single phase with spatially uniform bulk transport properties, such as electrical and thermal conductivities. The validity of this assumption will be tested in the following section by direct comparison with the experimental data provided by the manufacturer, as well as with other studies reported in literature. We should note, however, that the random-walk algorithm can be readily adjusted to account for two (or even more) conductive phases with distinct bulk phase properties (e.g. see Schwartz et al. [31]), thus also allowing for modeling the effects of hydrophobic agents, such as PTFE treatment.

Fig. 8(a) and (b) show the effective in-plane, $\sigma_\parallel/\sigma_0$, and through-plane, $\sigma_\perp/\sigma_0$, conductivies, respectively, over the bulk phase value of the fibrous skeleton for various values of β in the absence of resin, namely for $\chi = 0$. Besides the expected result of equal $\sigma_\parallel$ and $\sigma_\perp$ values for the case of an isotropic skeleton (namely, for $\beta = 1$), we observe that these values depend strongly on the anisotropy of the medium, with an increase of $\sigma_\parallel$ coupled with a significant decrease of $\sigma_\perp$ (more than an order of magnitude), as β increases and the fibers align in the xy-plane. This sharp decrease of through-plane conductivities should be viewed under the prism of percolation theory. Given that the percolation threshold in the through-plane direction depends on the average length of the fibers in this direction (projection of the fibers along the z-axis), besides the number density of fibers in the domain and the fiber diameter [32,33], we expect that the through-plane conductivity will exhibit a power-law decrease as the solid phase fraction $(1-\varepsilon)$ becomes progressively equal to its critical value $(1-\varepsilon_c)$, namely $\sigma_\perp \propto (\varepsilon_c - \varepsilon)^t$ for $\varepsilon < \varepsilon_c$, where $t > 0$ is a critical exponent [34]. The effect of porosity is in fact more pronounced in more anisotropic structures, e.g. a two-orders of magnitude decrease is observed for a change of ε from 0.75 to 0.9, as shown for $\beta = 10^2$ in Fig. 8(b), since the percolation threshold ε_c for the through-plane conductivity is expected to become lower as the fibers align in the xy-plane.

The effects of resin content are depicted in Fig. 8(c) and (d). It is interesting to note that the presence of binder, even at low quantities, typically increases the effective medium conductivity in both directions. This should be largely anticipated, as resin deposits on top of fiber surfaces (acting a wetting fluid prior to graphitization), thus increasing their apparent radius, as well as in fiber intersections, thus increasing their cross-sectional area. For these reasons, the effects of fiber content are more profound in the through-plane direction, where electrons (or heat) are transferred primarily at interactions between neighboring fibers, while the effect is marginal in the in-plane direction, where it should primarily attributed to the increased apparent fiber radii.

These effects are also demonstrated in Fig. 8(e) and (f) that show the ratio of conductivities, $\sigma_\parallel/\sigma_\perp$, for zero (e) and 20% (f) resin content. For the case of 20% resin, the significant increase of the through-plane component results in a decrease by a factor of 2 in the ratios over the entire range of porosities and anisotropy parameter values. This further highlights the important contribution of resin to the effective transport properties of GDL's in PEM FCs (besides its contribution to the structural strength of the composite under mechanical stress), allowing for enhanced heat and electron transfer from the catalytic layers towards the highly conductive bipolar planes.

6. Comparison with experimental data

We conclude our study with a direct comparison of our numerical results for both the reconstructed and X-ray computed domains with experimental results available in the literature. For this purpose, it was necessary to obtain some estimate for the values of parameters β and χ, that are used for the stochastic reconstruction of the composite, besides the medium porosity ε, which has been measured equal to $\varepsilon = 0.78 \pm 0.01$ using X-ray μ-CT (in agreement with the value $\varepsilon = 0.78$ reported by the manufacturer).

Regarding the resin content in the finished graphitized product, χ, the paper fabrication process, as described by Mathias et [2], implies that it should lie in the range 10–30% w/w. Furthermore, a rough estimate for the value of the anisotropy parameter can be obtained directly from our X-ray measurements, which have shown that $\beta \geq 5.0$, as discussed in the previous sections. A comparison, however, of this result for the effective conductivities of the medium with the values provided by the manufacturer suggests that the medium anisotropy should be somehow higher and in the range of $10 \leq \beta \leq 10^2$, where the ratio of in- to through-plane conductivities lies in the range of $8 \leq \frac{\sigma_\parallel}{\sigma_\perp} \leq 14$ for χ=0.2 (Fig. 8(f)). This is deduced by comparing with the ratio of thermal and electrical conductivities provided by Toray Inc, namely $\frac{k_\parallel}{k_\perp} = 12.35$ and $\frac{\sigma_\parallel}{\sigma_\perp} = 14.29$, respectively (see Table 1).

Table 1 presents an overview of the transport properties provided by the manufacturer for Toray TGP-H-090 carbon paper [24], and other experimentally determined values from the literature, compared to our numerical simulations in reconstructed domains with $\varepsilon = 0.78$, $\beta = 10^2$ and $\chi = 0.2$, and the X-ray computed domains. In general, our results compare remarkably well with the available experimental data for all transport properties studied, with the notable exception of effective diffusivities, that are found typically higher compared to the literature. We should note however that the reported experimental values for the latter property rely on a series of oversimplified calculations, such as the assumption of zero H_2 concentration on the catalyst side of the GDL [9], or the combination of diffusive and convective mass transfer [35] within the GDL, that could lead to an underestimation of the calculated effective diffusivities. Indeed, the experimental values reported in the literature, ranging from $0.21 \leq \frac{D_\perp}{D_0} \leq 0.38$ and $0.48 \leq \frac{D_\parallel}{D_0} \leq 0.58$, appear to be quite low for a material with such a high porosity, as GDLs, and should be also compared against the significantly higher value of $\frac{D_\varepsilon}{D_0} \approx 0.67$, reported for dense sphere

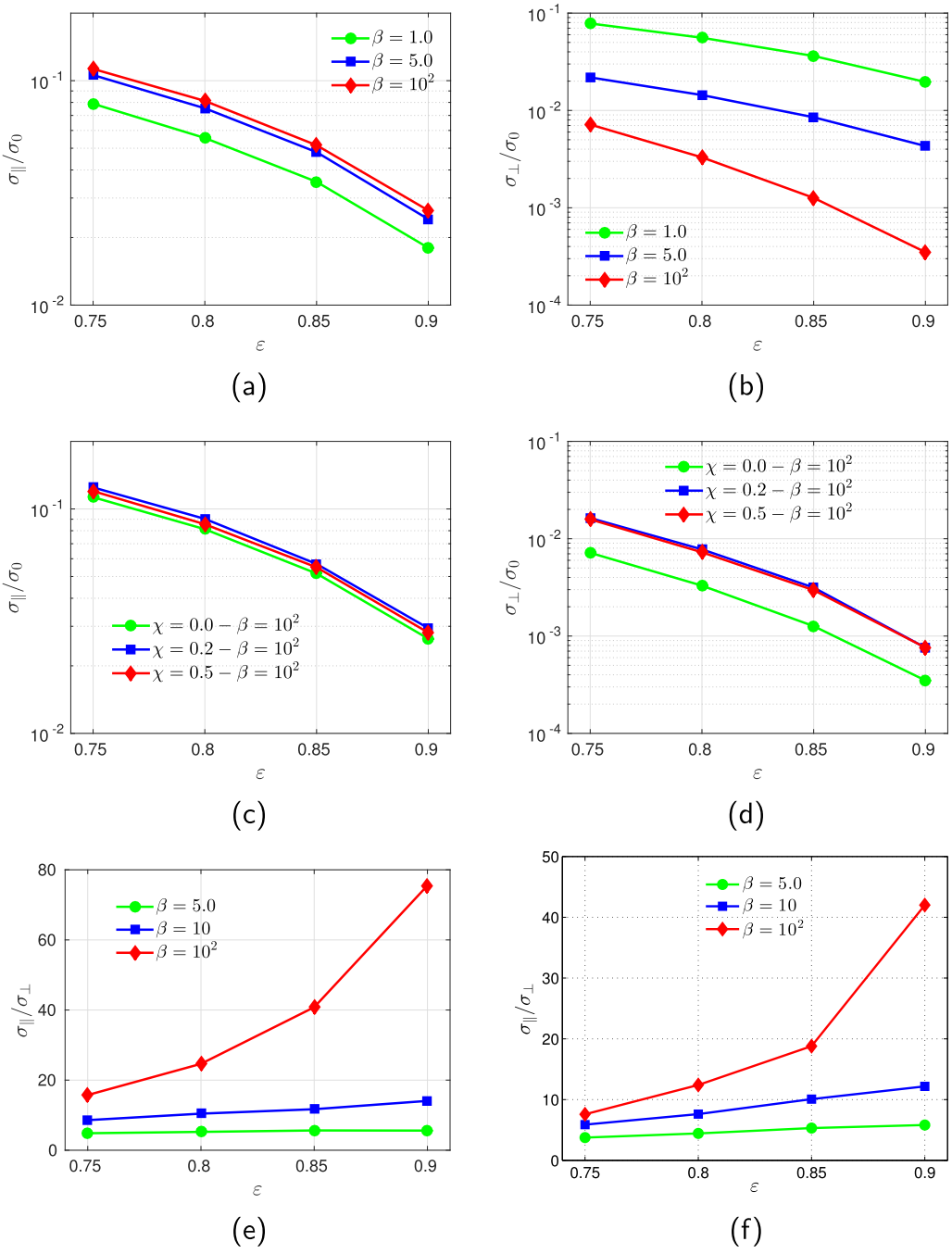

Fig. 8. (a)-(b) Calculated in-plane and through-plane effective conductivities (electrical and thermal) of the fiber skeleton (prior to resin deposition, thus $\chi = 0$) as a function of porosity, ε, and for different values of the anisotropy parameter, β. The values are averaged over 4 different fibrous domains and the maximum error for the entire data set is less than 5.6%. (c)-(d) Effective conductivities of the composite material (fibers + resin) for different values of the resin content, χ, and $\beta = 10^2$. (e)-(f) Effective conductivity ratios of the composite material for different values of β, and (e) 0% and (f) 20% resin content.

packings with porosities $\varepsilon \approx 0.37$ [36] (a porous medium with almost half the porosity of Toray C-fiber paper). We thus believe that the values calculated with our simulations should be closer to the actual ones of the medium. This particular point, however, deserves further investigation.

The striking similarity between the ratios of both electrical and thermal conductivities, as reported by Toray Inc (see Table 1), also suggests that the composite medium actually behaves as a single phase component after graphitization, with spatially uniform bulk phase transport properties in both the fibrous skeleton and the resin. In this sense, the calculated values for the effective to bulk phase conductivity ratios can be combined with the effective conductivities provided by the manufacturer, in order to deduce the bulk phase properties of the composite, either σ_0 or k_0. Using thus the values of Fig. 8(c)-(b) for $\chi = 0.2$, $\beta = 10^2$ and $\varepsilon = 0.78$, we conclude that $1.23 \times 10^5 \leq \sigma_0 \leq 1.74 \times 10^5$S/m. Likewise, the bulk phase thermal conductivity is found to be in the range $168 \leq k_0 \leq 204$W/mK. Both these bulk phase values are in good agreement with the expected properties of pure natural Graphite, $\sigma_{0,g} = 1 - 2 \times 10^5$ S/m and $k_{0,g} = 50 - 400$ W/mK [37,38]. As

Table 1
Experimentally determined transport properties of Toray TGP-H-090 and comparison with numerical simulations.

		Toray data [24]	Literature	Numerical results stochastic domain $\beta = 10^2$, $\chi = 0.2$, $\varepsilon = 0.78$	Numerical results X-ray domain
Permeability	$K_\perp$	8.5×10^{-12} m^2	8.99×10^{-12} m^2 ([6])	8.5×10^{-12} m^2	8.0×10^{-12} m^2
	$K_\parallel$		12.7×10^{-12} m^2[a] ([6])	12.6×10^{-12}m^2	14.1×10^{-12} m^2
	$K_\parallel/K_\perp$		1.41	1.48	1.76
Diffusivity	$D_\perp/D_0$		0.21[b] ([35]), 0.34[c] ([41,9]), 0.38[d] ([21])	0.55	0.52
	$D_\parallel/D_0$		0.48[b] ([42]),0.58[d] ([21])	0.65	0.61
	$D_\parallel/D_\perp$		1.26–2.76	1.18	1.17
Thermal conductivity	$k_\perp$	1.7 W/m K	1.8 W/m K [7]	1.88 W/m K[g]	2.8 W/m K[g]
	$k_\parallel$	21 W/m K	17.5 W/m K[c] [43]	19.0 W/m K[g]	15.8 W/m K[g]
	$k_\parallel/k_\perp$	12.35	9.72	10.23	5.70
Electrical conductivity	$\sigma_\perp$	1.25×10^3 S/m	1.5×10^3S/m[e] [21]	1.5×10^3S/m[f]	2.6×10^3S/m[f]
	$\sigma_\parallel$	17.86×10^3 S/m	12×10^3 S/m[e] [21]	15.1×10^3 S/m[f]	14.8×10^3 S/m[f]
	$\sigma_\parallel/\sigma_\perp$	14.29	8.00	10.23	5.70

[a] Value obtained from Carman-Kozeny equation for $\varepsilon = 0.78$ and fiber diameter $d_f = 9.2$ μm.
[b] Value for Toray 90 with $\varepsilon \approx 0.76$.
[c] Value for Toray 120 with $\varepsilon \approx 0.75$.
[d] Extrapolated value from experimental data of Toray 60 with $\varepsilon \approx 0.78$.
[e] Value for Toray 60 with $\varepsilon \approx 0.78$.
[f] Value calculated assuming $\overline{\sigma}_0 = 1.48 \times 10^5$S/m.
[g] Value calculated assuming $\overline{k}_0 = 186$W/mK.

expected, these values are close to an order of magnitude higher than those of the carbonized PAN fibers (e.g. T300 by Toray) ($\sigma_{0,f} = 0.59 \times 10^5$ S/m and $k_{0,f} = 10 - 20$ W/mK) that are used for the manufacturing of the graphitized C-fiber paper composite [39,5].

The average bulk phase thermal and electrical conductivities, $\overline{k}_0 = 186$W/mK and $\overline{\sigma}_0 = 1.48 \times 10^5$S/m, respectively, are then used to calculate the effective transport properties of the stochastically reconstructed structures and the X-ray domains, given the corresponding ratios obtained with the random walk method, as shown in Table 1. While the values for the effective thermal and electrical conductivities (both in- and through-plane) of the stochastic reconstructed domains are in very good agreement with those reported by the manufacturer and in the literature, the through-plane values for the X-ray domains are quite larger. This could be due to the thresholding algorithm used to generate the binarized domains from the X-ray image stack and the high sensitivity of the through-plane conductivities to the calculated resin content, as also shown in Fig. 8(d).

The GDL reconstruction approach proposed in this work can also be compared with those of earlier studies that relied on the morphological opening approach for the spatial distribution of resin. El Hannach and Kjeang [20], for instance, also studied the transport properties of carbon-based GDLs at the microscale, based on a fiber deposition methodology that ensures the generation of non-overlapping fibers. The respective methodology was complemented by a variant of the morphological opening algorithm that preferably turned smaller pore voxels into resin voxels until the desired porosity was achieved. Moreover, fibers and resin were treated as distinct phases with significantly different bulk phase transport properties (a ratio of 6.4 for the fiber to resin bulk phase electrical conductivies, and a ratio of 3.4 for the corresponding thermal conductivity ratio). In this way, the authors introduced the above extra adjustable parameters (two more parameters than those of the methodology proposed here) to match their numerical results with the corresponding experimental values from the literature. Our methodology, however, relies on a resin deposition algorithm that pursues the minimization of the resin-void-fiber interfacial energy, thus producing thermodynamically consistent solutions for the spatial distribution of phases. In this sense, this approach should be considered as a more generic superset of the morphological opening model, as it can provide resin phase distributions with different fiber-resin contact angles, depending on the parameters used for Young's equation (Eq. (5)).

Regarding the bulk phase properties of the composite, our approach relies on the Toray carbon-paper fabrication process, as presented by Mathias et al. [2], indicating that both the fiber and resin phases are to some extent graphitized during the last production step, thus yielding practically similar bulk phase transport properties. This assumption is also strongly supported by the in- to through-plane thermal and electrical conductivity ratios, as reported by Toray Inc, which are practically equal (see Table 1). We should also note that the proposed medium characterisation methodology can be readily extended to account for the effects of hydrophobic agents, e.g. PTFE treatment, and/or ungraphitized resin on the effective transport properties of the finished product, by appropriately adjusting the random-walk model to account for two (or even more) conductive phases with distinct bulk phase properties (see e.g. Schwartz et al. [31].)

7. Conclusions

In this work we proposed a novel process-based methodology for the stochastic reconstruction of Carbon fiber-based papers, which are commonly used as Gas Diffusion Layers in PEM fuel cells. The model relied on the standard method for the anisotropic deposition of carbon fibers, in combination, however, with a rigorous model for the spatial distribution of the graphitized thermoset resin, that is typically applied to enhance the structural robustness and thermal/electrical conductivities of the composite material. We presented an extensive numerical study of the most important transport properties of such materials, including Darcy permeabilities, effective diffusivities, thermal/electrical conductivities and void tortuosity, by modeling transport phenomena at the microscale, both within the porous space (void) and the solid skeleton of the stochastically reconstructed structures, as well as in binarized μ-CT domains. Our results focused primarily on the effects of the medium's porosity, anisotropy and resin content on the above calculated properties. The proposed reconstruction and characterisation methodology captures quite satisfactorily the entire range of experimentally determined properties of Toray 090 carbon paper for reasonable values of the model parameters.

Acknowledgements

This work was partially supported by the European Union under the H2FC (FP7-Capacities, Grant Agreement Number 284522) and the EnTeC programme (FP7-REGPOT-20122013-1, Grant Agreement Number 316173).

Appendix A. Numerical model for the reconstruction of the fibrous skeleton

We present below in detail the digital reconstruction algorithm for the formation of the fiber skeleton (prior to resin deposition) in a discrete 3D domain of size L^3. As also discussed above, the fibrous skeleton consists of randomly distributed overlapping cylindrical segments of radius R with orientations that follow a certain probability distribution. Each segment is characterized by a random point along its principal axis with position vector $\vec{r}_0 = (x_0, y_0, y_0)$ and a unit vector $\vec{n} = (n_x, n_y, n_z)$ parallel to the principal axis. The axis under consideration is thus described by the following parametric equation;

$$\vec{r}(s) = \vec{r}_0 + \vec{n}s \tag{17}$$

where $s \in R$, while the directional cosines of the unit vector can be expressed as;

$$\begin{aligned} n_x &= \sin\theta\cos\phi \\ n_y &= \sin\theta\sin\phi \\ n_z &= \cos\theta \end{aligned} \tag{18}$$

where $n_x^2 + n_y^2 + n_z^2 = 1$ and $\theta \in [0,\pi]$, $\phi \in [0,2\pi]$ are the polar and azimuthal angles, respectively.

Imposing the condition that the direction of the principal axis is uniformly distributed in the $xy-$ plane, ϕ is chosen randomly and uniformly in the range $[0,2\pi]$ the probability density function reads;

$$p_{xy}(\phi) = \frac{1}{2\pi}. \tag{19}$$

The probability density for the polar angle is;

$$p_z(\theta) = \frac{\beta\sin\theta}{2\left[1 + \left(\beta^2 - 1\right)\cos^2\theta\right]^{\frac{3}{2}}}. \tag{20}$$

Eq. (20) is derived by considering the following general probability expression proposed by Schladitz [23] in combination with Eq. (19);

$$p(\theta,\phi) = p_z(\theta)p_{xy}(\phi) = \frac{\beta\sin\theta}{4\pi\left[1 + \left(\beta^2 - 1\right)\cos^2\theta\right]^{\frac{3}{2}}}. \tag{21}$$

In a similar fashion, the probability density function for the position vector of the random point that belongs to the principal axis of each cylindrical segment $\vec{r_0} = (x_0, y_0, z_0)$ can be expressed as;

$$p_0 = \frac{1}{L} \tag{22}$$

for each vector component, x_0,y_0 and z_0.

The generation of random numbers, ζ, that follow the above probability density functions for $\vec{r}_0$, ϕ and θ can be achieved using the inversion method [40]. This method is based on the calculation of the cumulative distribution function $\mathcal{P}(\zeta) = \int_a^{\zeta<b} p(\zeta')d\zeta'$ for each probability function, $p(\zeta)$, where $\zeta \in (a,b)$. (Note here that $\mathcal{P}(\zeta) \in (a,b)$). We can then define the inverse of the cumulative density function as follows;

$$\zeta = \mathcal{P}^{-1}(\xi) \tag{23}$$

where ξ is an auxiliary variable that takes values in the range (0,1). A sequence of random values that follow a uniform distribution in the range (0,1) are produced computationally for the auxiliary variable ξ using a pseudo-random number routine. These values are used as input in Eq. (23) to produce the required random ζ values. The ζ values obtained with the above method follow the probability density function, $p(\zeta)$.

Applying the aforementioned method, the generation of uniform random numbers for the position vector $(x_0,y_0,z_0) \in (0,L)^3$ and the azimuthal angle $\phi \in (0,2\pi)$ is obtained by;

$$(x_0, y_0, z_0) = \left(L\xi_x, L\xi_y, L\xi_z\right) \tag{24}$$

and

$$\phi = 2\pi\xi_\phi \tag{25}$$

respectively, where ξ_x,ξ_y,ξ_z,$\xi_\phi \in (0,1)$ are the random values obtained by the pseudo-random number routine.

In a similar fashion, for the generation of random values for the polar angle $\theta \in (0,\pi)$ (which follows the probability density function of Eq. (21)), we first obtain the cumulative distribution of θ, $P_z(\theta)$:s

$$\begin{aligned} P_z(\theta) &= \int_0^\theta \frac{\beta\sin t}{2\left[1 - \left(\beta^2 - 1\right)\cos^2 t\right]^{\frac{3}{2}}}dt \\ &= \frac{1}{2} - \frac{\beta\cos\theta}{2\sqrt{\left(\beta^2 - 1\right)\cos^2\theta + 1}} \end{aligned} \tag{26}$$

The inverse function, $P_z^{-1}(\xi_\theta)$, is then:

$$\theta = P_z^{-1}(\xi_\theta) = \pm\arccos\left[\sqrt{\frac{1}{\frac{\beta^2}{(1-2\xi_\theta)^2} - \beta^2 + 1}}\right] \tag{27}$$

Thus, starting from a set of pseudo-random values $(\xi_x,\xi_y,\xi_z,\xi_\theta,\xi_\phi)$, we repeate the above procedure to generate a series of straight lines (corresponding to the principal axes of the cylindrical segments) characterized by the position vector $\vec{r}_0 = \vec{r}_0(\xi_x, \xi_y, \xi_z)$ and a parallel unit vector $\vec{n} = \vec{n}(\xi_\theta, \xi_\phi)$. Assuming that we have M such lines ($\vec{r}_{0,m}$ and $\vec{n}_m$, $m = 1,2, \ldots,M$), the points that belong to the cylindrical segments (and thus to the fibrous skeleton) can be defined through the position vector $\vec{r}_c = (x_c, y_c, z_c) \in (0, L)^3$, whose distance, d, from at least one principal axis of the above series satisfies the condition $d \le R$, or equivalently;

$$d = \left|\left(\vec{r}_c - \vec{r}_{0,m}\right) \times \vec{n}_m\right| \le R. \tag{28}$$

Finally, in order to produce a discrete digital domain, the continuous space L^3 is divided in N^3 cubic voxels, with a characteristic size $\delta x = L/N$. The coordinates of the center of each voxel is $\vec{r}_{ijk} = ((i-1/2)\delta x, (j-1/2)\delta x, (k-1/2)\delta x)$ with $i = 1,2, \ldots,N$, $j = 1,2, \ldots,N$, $k = 1,2, \ldots,N$. The phase of each voxel is determined by substituting in Eq. (28) the $\vec{r}_c$ by the corresponding $\vec{r}_{ijk}$.

In summary the overall procedure is:

1. Obtain random points, $\vec{r}_{0,m} \in (0, L)^3$, and the corresponding random directions, $\vec{n}_m$ for every one of M cylindrical segments.

The random points and the directions are chosen according to the corresponding probability density functions as described above.
2. Discretize the domain in N^3 cubic voxels. The voxels are taken to be solid if their center satisfies Eq. (28) for at least one principal axis (out of the total M axes). The remaining voxels are taken to be void.
3. Determine the porosity and if necessary adjust R and/or M in order to match the required porosity.

Appendix B. Lattice Boltzmann model for the calculation of the velocity profile.

Using a convenient discretization of the continuous Boltzmann equation in time, space and microscopic velocity space, the evolution equation for the particle distribution function with the Bhatnagar-Gross-Krook approximation in the presence of a body force density $\vec{G}$ reads [26];

$$f_i(\vec{x}+\vec{e}_i\delta t, t+\delta t) - f_i(\vec{x},t) = -\frac{1}{\tau_0}\left(f_i(\vec{x},t) - f_i^{eq}(\vec{x},t)\right) + \delta t F_i(\vec{x},t) \tag{29}$$

where $\vec{e}_i$ are the microscopic velocity components, δt is the time step and τ_0 is a non-dimensional relaxation time related to the kinematic fluid viscosity as;

$$\nu_0 = c_s^2\delta t(\tau_0 - 0.5) \tag{30}$$

The parameter c_s is the lattice speed of sound, which for a typical 3D domain with 19 microscopic velocity components $\vec{e}_i$ (commonly reffered to as a D3Q19 discretization) takes a value equal to $c_s^2 = \frac{1}{3}\left(\frac{\delta x}{\delta t}\right)^2$.

The dicretized equilibrium distribution function is;

$$f_i^{eq}(\vec{x},t) = w_i\rho(\vec{x},t)\left(1 + \frac{\vec{e}_i\cdot\vec{u}(\vec{x},t)}{c_s^2} + \frac{(\vec{e}_i\cdot\vec{u}(\vec{x},t))^2}{2c_s^4} + \frac{\vec{u}(\vec{x},t)\cdot\vec{u}(\vec{x},t)}{2c_s^2}\right) \tag{31}$$

The forcing term in discrete format reads;

$$F_i(\vec{x},t) = w_i\left(1-\frac{1}{2\tau_0}\right)\left(\frac{\vec{e}_i - \vec{u}(\vec{x},t)}{c_s^2} + \frac{\vec{e}_i\cdot\vec{u}(\vec{x},t)}{c_s^4}\vec{e}_i\right)\cdot\vec{G} \tag{32}$$

The weight factors, w_i, for the D3Q19 scheme read;

$$w_i = \begin{cases} 1/3 & : i = 0 \\ 1/18 & : i = 1,2,\ldots,6 \\ 1/36 & : i = 7,8,\ldots,18 \end{cases} \tag{33}$$

The microscopic velocity components read;

$$\vec{e}_i = \begin{cases} (0,0,0)c & & & : i = 0 \\ (\pm1,0,0)c & (0,\pm1,0)c & (0,0,\pm1)c & : i = 1,2,\ldots,6 \\ (\pm1,\pm1,0)c & (\pm1,0,\pm1)c & (0,\pm1,\pm1)c & : i = 7,8,\ldots,18 \end{cases} \tag{34}$$

The macroscopic mass and momentum densities are then obtained by integrating along the microscopic velocity space, $\vec{e}_i$;

$$\rho(\vec{x},t) = \sum_{i=0}^{q} f_i(\vec{x},t) \tag{35}$$

and

$$\rho(\vec{x},t)\vec{u}(\vec{x},t) = \sum_{i=0}^{q}\vec{e}_i f_i(\vec{x},t) + \frac{\delta t}{2}\vec{G} \tag{36}$$

References

[1] S. Kocha, in: W. Vielstich, H.A. Gasteiger, A. Lamm, H. Yokokawa (Eds.), Handbook of Fuel Cells, John Wiley and Sons, 2010.
[2] M. Mathias, J. Roth, J. Fleming, W. Lehnert, in: W. Vielstich, H.A. Gasteiger, A. Lamm, H. Yokokawa (Eds.), Handbook of Fuel Cells, John Wiley and Sons, 2010.
[3] U. Pasaogullari, in: W. Vielstich, H.A. Gasteiger, A. Lamm, H. Yokokawa (Eds.), Handbook of Fuel Cells, John Wiley and Sons, 2010.
[4] S. Park, J.-W. Lee, B.N. Popov, Int. J. Hydrogen Energy 37 (2012) 5850–5865.
[5] P.J. Walsh, in: ASM Handbook, vol. 21, ASM international, 2001.
[6] J.T. Gostick, M.W. Fowler, M.D. Pritzker, M.A. Ioannidis, L.M. Behra, J. Power Sources 162 (2006) 228–238.
[7] M. Khandelwal, M. Mench, J. Power Sources 161 (2006) 1106–1115.
[8] M. Ismail, T. Damjanovic, D. Ingham, M. Pourkashanian, A. Westwood, J. Power Sources 195 (2010) 2700–2708.
[9] G. Hwang, A. Weber, J. Electrochem. Soc. 159 (2012) F683–F692.
[10] N. Alhazmi, M. Ismail, D. Ingham, K. Hughes, L. Ma, M. Pourkashanian, J. Power Sources 241 (2013) 136–145.
[11] H. Sadeghifar, N. Djilali, M. Bahrami, J. Power Sources 248 (2014) 632–641.
[12] J. Yablecki, A. Bazylak, J. Power Sources 217 (2012) 470–478.
[13] J. Yablecki, A. Nabovati, A. Bazylak, J. Electrochem. Soc. 159 (2012) B647–B653.
[14] O. Chapuis, M. Prat, M. Quintard, E. Chane-Kane, O. Guillot, N. Mayer, J. Power Sources 178 (2008) 258–268.
[15] G. Luo, Y. Ji, C.-Y. Wang, P.K. Sinha, Electrochim. Acta 55 (2010) 5332–5341.
[16] J.T. Gostick, J. Electrochem. Soc. 160 (2013) F731–F743.
[17] V.P. Schulz, J. Becker, A. Wiegmann, P.P. Mukherjee, C.-Y. Wang, J. Electrochem. Soc. 154 (2007) B419–B426.
[18] A. Tamayol, K. Wong, M. Bahrami, Phys. Rev. E 85 (2012) 026318.
[19] N. Zamel, X. Li, J. Shen, J. Becker, A. Wiegmann, Chem. Eng. Sci. 65 (2010) 3994–4006.
[20] M. El Hannach, E. Kjeang, J. Electrochem. Soc. 161 (2014) F951–F960.
[21] J. Becker, R. Flückiger, M. Reum, F.N. Büchi, F. Marone, M. Stampanoni, J. Electrochem. Soc. 156 (2009) B1175–B1181.
[22] M.M. Daino, S.G. Kandlikar, Int. J. Hydrogen Energy 37 (2012) 5180–5189 (Optimization Approaches to Hydrogen Logistics).
[23] K. Schladitz, S. Peters, D. Reinel-Bitzer, A. Wiegmann, J. Ohser, Comput. Mater. Sci. 38 (2006) 56–66.
[24] Toray Instustries Inc, Toray carbon paper, 2015.
[25] S. Kirkpatrick, C.D. Gelatt, M.P. Vecchi, Science 220 (1983) 671–680.
[26] Z. Guo, C. Zheng, B. Shi, Phys. Rev. E 65 (2002) 046308.
[27] L.M. Schwartz, J.R. Banavar, Phys. Rev. B 39 (1989) 11965–11970.
[28] I. Ginzburg, D. d'Humières, Phys. Rev. E 68 (2003) 066614.
[29] M. Tomadakis, T.J. Robertson, J. Compos. Mater. 39 (2005) 163–188.
[30] M.M. Tomadakis, S.V. Sotirchos, AIChE J. 39 (1993) 397–412.
[31] L.M. Schwartz, E.J. Garboczi, D.P. Bentz, J. Appl. Phys. 78 (1995) 5898–5908.
[32] I. Balberg, C.H. Anderson, S. Alexander, N. Wagner, Phys. Rev. B 30 (1984) 3933–3943.
[33] L. Berhan, A.M. Sastry, Phys. Rev. E 75 (2007) 041120.
[34] S.H. Foulger, J. Appl, Polym. Sci. 72 (1999) 1573–1582.
[35] P. Mangal, L.M. Pant, N. Carrigy, M. Dumontier, V. Zingan, S. Mitra, M. Secanell, Electrochim. Acta 167 (2015) 160–171.
[36] D. Hlushkou, H. Liasneuski, U. Tallarek, S. Torquato, J. Appl. Phys. 118 (2015) 124901.
[37] R.A. Buerschaper, J. Appl. Phys. 15 (1944) 452–454.
[38] N. Deprez, D.S. McLachlan, J. Phys. D. 21 (1988) 101.
[39] Toray Standard Modules Carbon Fibers, Toray Instustries Inc, 2015.
[40] L. Devroye, Non-uniform Random Variate Generation, Springer-Verlag, 1986.
[41] N. Zamel, N.G. Astrath, X. Li, J. Shen, J. Zhou, F.B. Astrath, H. Wang, Z.-S. Liu, Chem. Eng. Sci. 65 (2010) 931–937.
[42] N. Carrigy, M. Secanell, ECS Trans. 64 (2014) 487–499.
[43] E. Sadeghi, N. Djilali, M. Bahrami, J. Power Sources 196 (2011) 3565–3571.